UC Santa Cruz

UC Santa Cruz Previously Published Works

Title

Effects of annealing on phase transformation and corrosion mechanism of severely deformed Al0.3CoCrFeNi high-entropy alloy

Permalink

https://escholarship.org/uc/item/4x16k308

Journal

npj Materials Degradation, 10(1)

ISSN

2397-2106

Authors

Tsai, Fu-Yun

Pandaleon, Alice

O'Brien, Sean

et al.

Publication Date

2026-06-02

DOI

10.1038/s41529-026-00818-4

Copyright Information

This work is made available under the terms of a Creative Commons Attribution License, available at https://creativecommons.org/licenses/by/4.0/

Peer reviewed

eScholarship.org Powered by the California Digital Library
University of California

npj | materials degradation

Article

Published in partnership with CSCP and USTB

https://doi.org/10.1038/s41529-026-00818-4

Effects of annealing on phase transformation and corrosion mechanism of severely deformed $Al_{0.3}$CoCrFeNi high-entropy alloy

Check for updates

Fu-Yun Tsai[1], Alice Pandaleon[1], Sean O'Brien[1], Andrew Martin[1], Alana Pauls[1], Farhan Ishrak[1], Michael Lastovich[1], Md Jasim Uddin[1], Zengqing Zhuo[2], Jinghua Guo[2], Martin Mwangi Thuo[1], Rajeev Gupta[1], Rajarshi Banerjee[3], Elizabeth Kautz[4] & Bharat Gwalani[1] ✉

The effects of transitional phase states on corrosion behavior in the equiatomic-derived high-entropy alloy $Al_{0.3}$CoCrFeNi were investigated following 90% cold-rolling and subsequent isothermal annealing at 620 °C for durations ranging from 1 to 50 h. Electron and X-ray diffraction analysis reveal a progressive transformation from single-phase FCC to an FCC + B2 + σ trinity. Nano-scale B2 and σ nuclei emerge within partially recrystallized grains after 1–2 h, lowering the cold rolling micro-strain from 0.26 to 0.13. This heterogeneous state exhibits the maximum hardness (552 VHN) while enlarging the chloride-passive window by > 200 mV relative to the solutionized material. Prolonged annealing (> 10 h) coarsens the intermetallics and exhausts Al from the matrix, thereby reducing pitting resistance due to the loss of protective Al_2O_3 film. Characterization by electron microscopy and atom probe tomography reveals that Al-rich B2 nuclei are the primary Al sink that compromises Al_2O_3 formation at long times. The results demonstrate that a narrowly defined heat-treatment window balances strengthening with passivation in $Al_{0.3}$CoCrFeNi, providing a mechanistic blueprint for designing corrosion-tolerant high-entropy alloys (HEAs).

The fabrication and design of alloys in metallurgy have led to significant technological advancements across various industries (infrastructure, aerospace, automotive, etc.)[1–4], due to the ability to enhance and tailor specific properties of metals for particular applications. While traditional alloys are typically designed with one or two primary elements with minor additions of others, increasing the proportion of additional elements can result in the formation of brittle intermetallic compounds, which can reduce mechanical performance. The introduction of HEAs overcomes the limitations of traditional alloys by introducing many interacting elements in the system, which increases tunability and minimizes the detrimental influence of any single element within a system. HEAs typically incorporate five or more elements in near-equiatomic proportions (5–35 atomic percent each)[5,6]. Recent research in HEAs has shown significant concurrent improvements in strength, ductility corrosion resistance, and high-temperature performance[3,4,7–10].

The $Al_{0.3}$CoCrFeNi alloy was developed as a derivative of the equiatomic CoCrFeNi system to enhance strength and corrosion resistance through the addition of aluminum. This system typically exhibits a multi-phase microstructure, including FCC, B2, and occasionally σ phases, which contribute to tunable mechanical properties[7,11]. Prior work[12] demonstrated that its tensile yield strength can be tailored from 160 MPa to 1800 MPa through thermomechanical processing alone, without altering composition.

The corrosion resistance of $Al_{0.3}$CoCrFeNi also shows promise in aggressive environments. Li et al.[13] reported that Al additions promote the formation of protective Al_2O_3 scales, while Firouzdor et al.[14] and Shi et al.[11] found that small Al additions (e.g., 0.3 at%) enhance passivation. However, excessive Al can promote BCC and B2 phase formation, which may reduce corrosion resistance and pitting stability[9]. Furthermore, Shi[9] noted that B2 phase presence diminishes pitting resistance, and studies by Zhang et al.[15]

[1]Department of Materials Science and Engineering, North Carolina State University, Raleigh, NC, USA. [2]Lawrence Berkeley National Lab, Berkeley, CA, USA. [3]Department of Materials Science and Engineering, University of North Texas, Denton, TX, USA. [4]Department of Nuclear Engineering, North Carolina State University, Raleigh, NC, USA. ✉e-mail: bgwalan@ncsu.edu

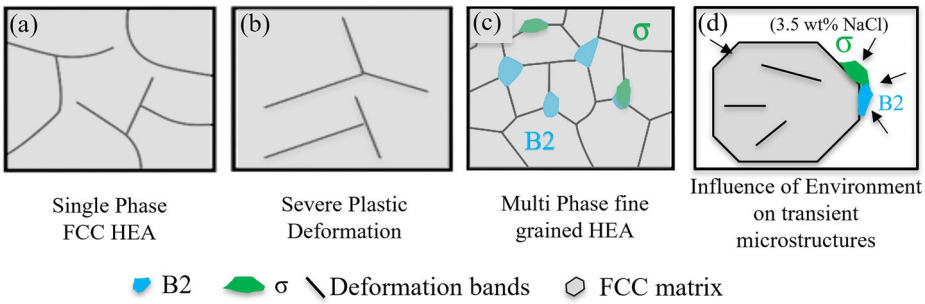


Fig. 1 | Conceptual map highlighting the largely unexplored link between transient microstructures in Al0.3CoCrFeNi alloy and their coupled strength–corrosion responses. a initial single-phase FCC matrix with coarse grains; **b** microstructural evolution under severe plastic deformation, showing the formation of high-density deformation bands; **c** multiphase fine-grained HEA structure showing precipitated B2 (blue) and σ (green) phases along the grain boundaries; and **d** schematic representation highlighting the influence of a corrosive environment (3.5 wt% NaCl) on the transient microstructures at the grain boundaries and phase interfaces.

and Qiu et al.[10] have shown that annealed conditions generally offer improved corrosion resistance compared to solutionized or remelted states.

These findings highlight $Al_{0.3}$CoCrFeNi as a promising alloy system for corrosion-resistant applications, particularly when phase composition and thermal history are carefully controlled.

Although several studies have examined corrosion mechanisms and passivity of HEAs in chloride environments[10,13,15–19], systematic investigations specifically linking annealing time, microstructural evolution, and corrosion resistance remain limited. In particular, few studies have explored how phase transformations affect oxide film formation during corrosion, or how the availability of key oxide-forming elements changes following these transformations. Moreover, the differences in oxide formation pathways and kinetics between highly deformed and fully or partially annealed HEAs are still not well understood. While many investigations focus on the effects of annealing temperature[11], the influence of annealing duration on phase transformations and subsequent passivation behavior has received comparatively little attention[20]. This study aims to address these gaps.

Figure 1 illustrates the dynamic interplay between microstructural evolution and environmental degradation in HEAs. Initially, the alloy exhibits a single-phase FCC structure formed by solutionizing, which transforms under cold rolling into a heavily deformed microstructure with elongated grains and high dislocation density. Annealing then promotes the formation of fine-grained multiphase structures with nanoscale B2 and σ precipitates. In corrosive environments such as 3.5 wt% (≈ 0.6 M) NaCl solution at near-neutral pH, ongoing microstructural changes—including recrystallization and precipitation—interact with corrosive processes, which may preferentially attack phase boundaries or precipitate-decorated grain boundaries. The schematic emphasizes how processing history dictates phase transformation pathways (highlighted in orange), while feedback loops from corrosion (indicated by black arrows) influence phase stability and degradation mechanisms. This schematic underscores the need to better understand the coupling between microstructure and corrosion to engineer HEAs with optimized performance under service conditions.

Hypothetically, the addition of Al into a multi-element mixture such as CoCrFeNi would alter the relaxation pathway of the alloy due to the influence and interaction of Al towards each of the other elements. Previously, Preferential Interactivity Parameter (PIP[21]) has shown that the oxidation affinity, size, standard reduction potential (E^0) and cohesive energy density (CED) control the speciation and surface formation of metal alloys and HEAs[22]. Thermodynamically, the addition of Al to the alloy increases the overall chemical driving force ($\langle \hat{T} \rangle$), particularly due to Al's strong affinity for certain elements. Even a minor addition (e.g., 0.3 at%) promotes interactions between Al and thermodynamically compatible elements to reduce system energy and approach pseudo-equilibrium under non-equilibrium conditions. Elements such as Ni and Cr are relatively close to Al on the PIP scale, making them more susceptible to Al-induced changes. These interactions can influence phase stability and relaxation behavior of Ni and Cr during thermal or corrosion processes.

In this study, $Al_{0.3}$CoCrFeNi alloy was subjected to high-temperature solid solution treatment, followed by 90% cold rolling and annealing at 620 °C for durations ranging from 1 to 50 h. With increasing annealing time, the microstructure evolved from a single-phase FCC structure to a multi-phase mixture containing FCC, B2, and sigma phases. While prior studies have associated such phase mixtures with improved strength and hardness[12], they may also compromise corrosion resistance[14,23]. Our findings reveal that short-term annealing (1–2 h) significantly enhances corrosion resistance, whereas extended annealing reduces it slightly, yet still maintains better performance than conventional stainless steel. This evolution in corrosion behavior is closely linked to the increasing presence of B2 and sigma phases and concurrent microstructural stress relief, as indicated by decreasing micro-strain. Notably, hardness increases up to 4 h of annealing before marginally declining, suggesting a trade-off between strengthening and corrosion resistance mechanisms.

Through this research, we demonstrate that appropriate heat treatment can achieve a desirable balance between strength and corrosion resistance in HEAs. The findings also provide insights into the transformation pathways influenced by prior sample conditions. This approach could be effectively applied to other HEAs and alloy systems.

Results and discussion

Microstructural evolution during 620 °C annealing

Figures S1, S2, and 2 collectively illustrate the microstructural evolution of the $Al_{0.3}$CoCrFeNi alloy after 90% cold rolling and subsequent annealing at 620 °C for varying durations (0, 10, and 50 h).

The unannealed sample (0 h, Fig. S1) exhibits a heavily deformed structure with elongated grains, high dislocation density, and no additional phase formation, indicative of severe plastic deformation. Upon annealing for 10 h (Fig. 2), the material shows the onset of recrystallization with more pronounced grain boundary contrast and the initial precipitation of secondary phases. EBSD analysis confirms the microstructure remains predominantly FCC (90%), but minor fractions of sigma (8%) and Al-Ni-rich (B2) (2%) phases are now present as shown in Fig. S2.

Further annealing to 50 h leads to a fully developed, coarser grain structure with well-defined precipitates located both at grain boundaries and within grains. Quantitatively, a dramatic phase transformation occurs: the FCC phase reduces significantly to 41%, while the sigma phase becomes dominant at 45%, and Al-Ni (B2) notably increases to 15% as shown in Fig. S2. The dominance of the Cr-rich σ phase in this state is typically associated with the formation of Cr-depleted zones and subsequent localized galvanic corrosion. This detrimental effect of theσ phase has been extensively documented in traditional stainless steels[24] as well as in other high-entropy alloy systems[25]. By contrast, our results for the 1–2 h samples suggest that these negative effects can be suppressed during the early, transient stages of precipitation.

Over estimation of sigma and B2 can be expected due to a lower confidence index in EBSD of these phases. However, the dramatic increase in phases fraction of these intermetallic is confirmed by additional TEM analysis. This indicates substantial growth and segregation of these secondary phases at the expense of the FCC matrix during prolonged annealing.

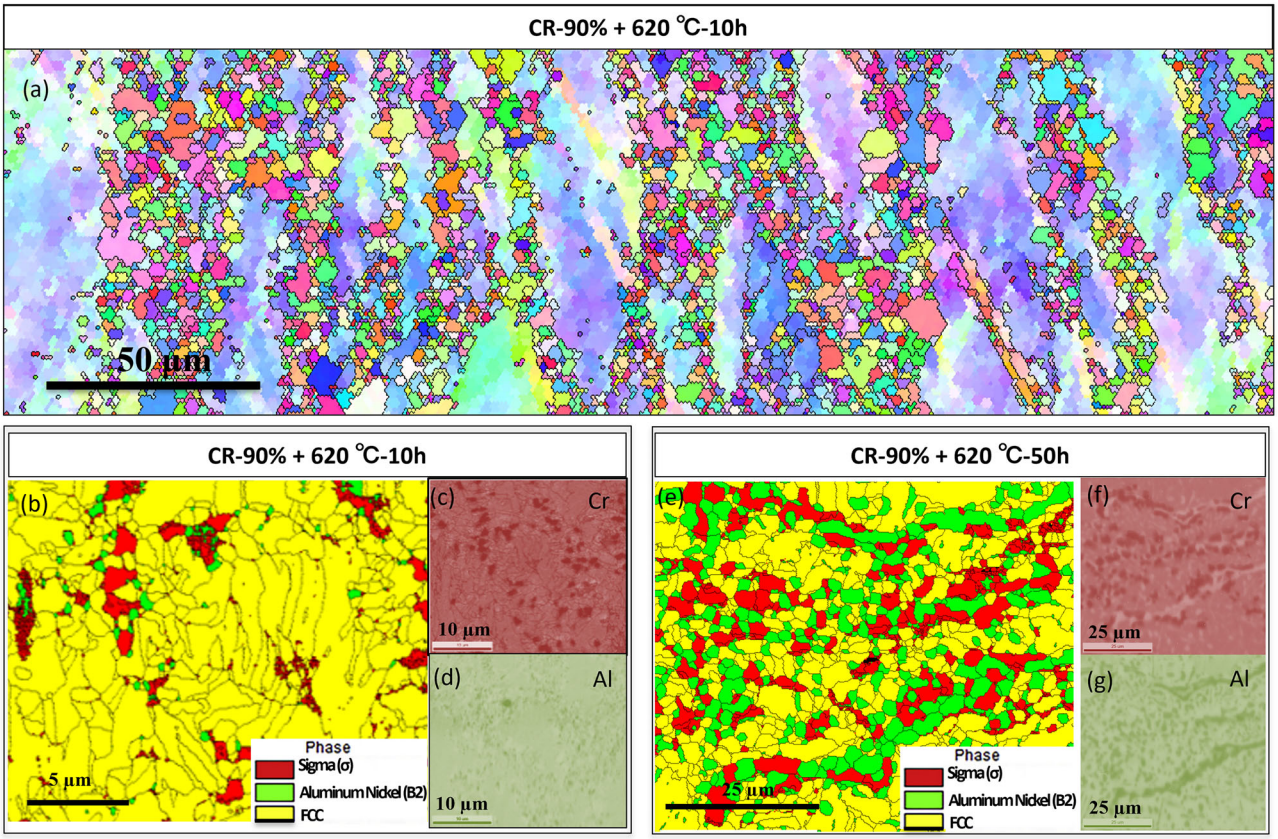


Fig. 2 | The 90% Cold rolled and annealed Al0.3CoCrFeNi alloy at 620 °C for 10 h and 50 h condition. a low-magnification Inverse Pole Figure (IPF) map; **b** phase map and **c** Cr map and **d** Al map for the 10 h condition; **e** phase map, **f** Cr map, and **g** Al map for the 50 h condition.

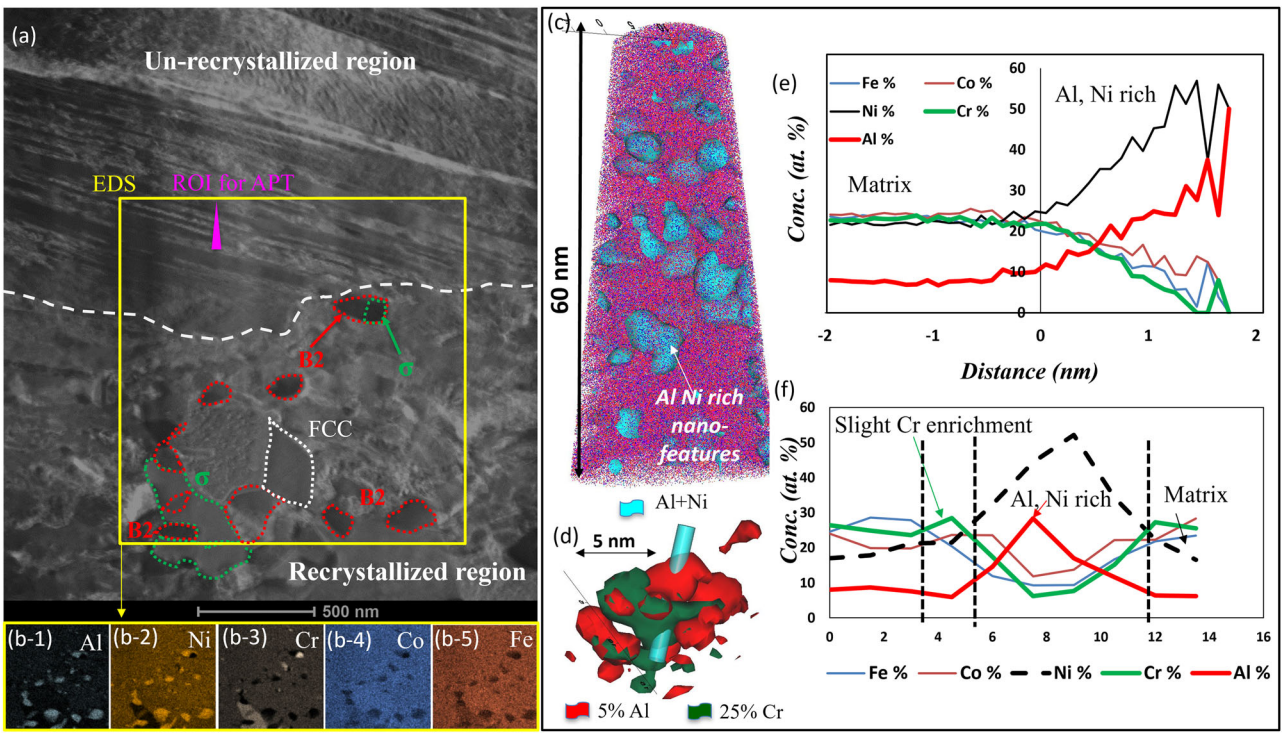


Fig. 3 | Early precipitation after 1 h anneal at 620 °C. a Bright-field TEM overview identifying recrystallised (R) and unrecrystallised (U) areas. **b1**–**b5** STEM-EDS maps from the boxed recrystallised grain revealing nano-scale B2 (Ni-Al-rich) and σ (Cr-rich) particles. **c** Isocomposition surfaces from the unrecrystallised region highlighted in (**a**). **d** Three-dimensional APT reconstruction (Al in red, Cr in green). **e** Proxigram across a representative Ni-Al domain. **f** One-dimensional concentration profile confirming Ni/Al and Cr partitioning.

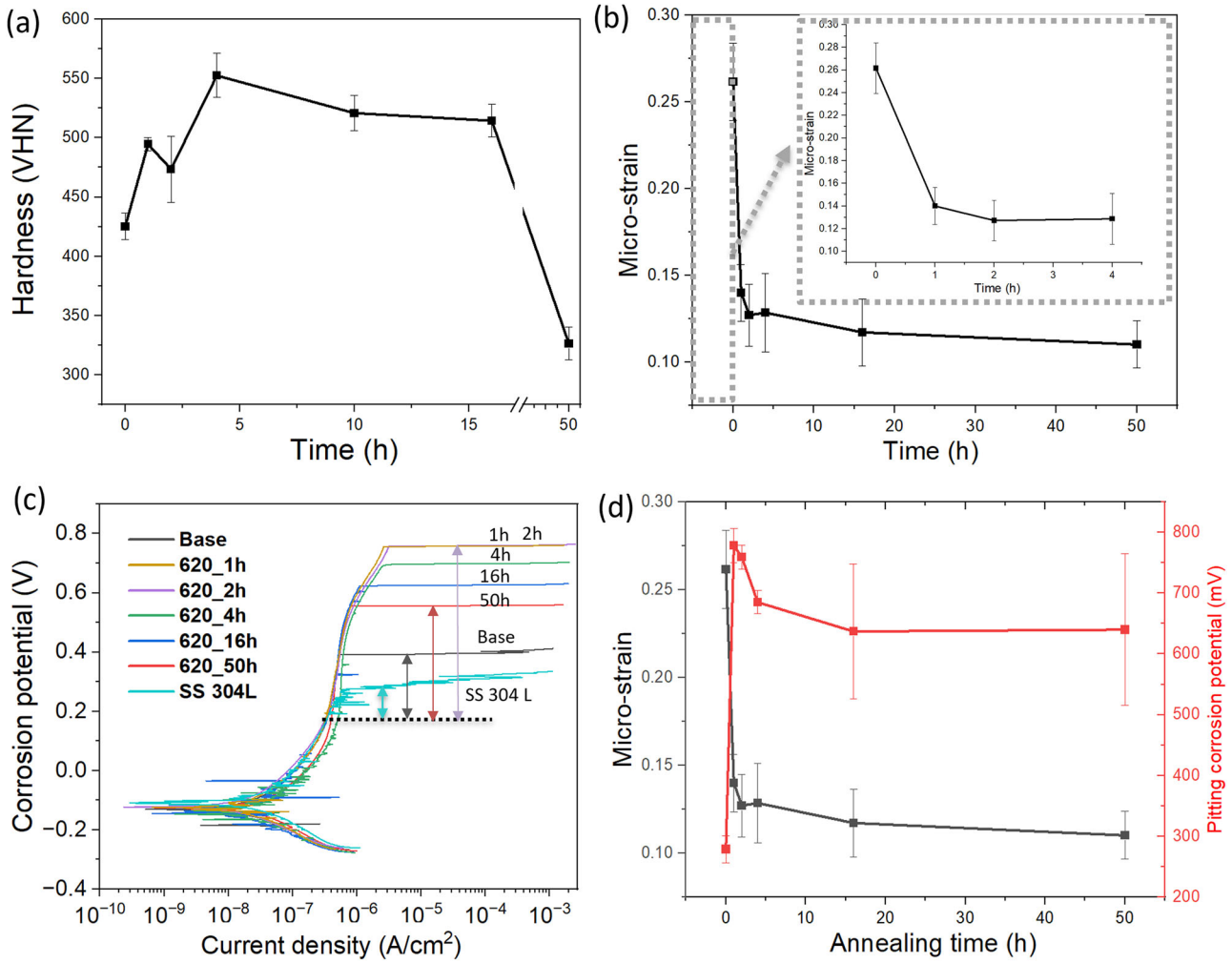


Fig. 4 | Property evolution with annealing time. a Vickers hardness versus time at 620 °C. **b** Root-mean-square lattice micro-strain determined by Williamson–Hall analysis. **c** Potentiodynamic polarisation curves recorded in 3.5 wt.% NaCl solution; "Base" = CR50 + 1100 C/1 h in recrystallized condition. **d** Correlation between micro-strain and pitting potential.

Early-stage precipitation revealed by correlative TEM–APT (1 h)

Figure 3 presents TEM and APT images of the $Al_{0.3}CoCrFeNi$ alloy under 90% cold rolling (CR90) followed by annealing at 620 °C for 1 h. As shown in Fig. 3 (a), TEM images reveal that the alloy exhibits regions of partial recrystallization, with some areas remaining unrecrystallized. Within the recrystallized regions, B2 (Ni/Al rich regions)and sigma phases (Cr rich region) are observed in (b-1) –(b-5). The APT images (shown in Fig. 3 (c–f)) provide detailed 3D structural information in the unrecrystallized region indicated as the region of interest (ROI) in (a). Isosurface are used to delineate Al rich (red in Fig. 3(d) and Cr rich (green in Fig. 3(d)) regions. Although B2 and sigma precipitates were not observed in the unrecrystallized region through TEM, APT results indicate the presence of domains rich in Ni and Al. These domains appear to act as nuclei for the formation of B2 phases, even though the precipitates are not visible in the TEM images. The line scan further confirms the presence of nuclei for both B2 and sigma phases. These nanoscale nuclei represent a transient, non-equilibrium kinetic trapping state in which Al has not yet been significantly consumed by B2 or σ. This preserves Al availability in the matrix, enabling rapid Al_2O_3 formation during corrosion.

APT also reveals sub-critical B2 nuclei in unrecrystallized regions, indicating early-stage partitioning not visible in TEM. The broader and more diffuse Al-depletion gradients around σ differ from classical Fe–Cr systems and reflect multicomponent diffusion unique to HEAs. These features provide direct evidence for kinetic trapping at short times and thermodynamic depletion at long times.

Hardness and lattice micro-strain

Figure 4(a) shows the hardness variation with annealing time. The hardness increases initially, peaking at 4 h due to partial recrystallization and the formation of nanoscale B2 and sigma precipitates, which hinder dislocation motion. Beyond 4 h, hardness decreases as the microstructure becomes more homogeneous and precipitates coarsen, reducing their effectiveness in strengthening.

Figure 4(b) illustrates microstrain measurements obtained via the Williamson-Hall method. The cold-rolled sample exhibits high microstrain due to plastic deformation. Annealing at 620 °C for 1 h significantly reduces microstrain, indicating partial recrystallization and phase transformation. Further annealing results in minimal changes in microstrain, suggesting stress relief and continued phase transformations.

Electrochemical behavior in 3.5 wt.% NaCl

The potentiodynamic polarization (PDP) curves for the $Al_{0.3}CoCrFeNi$ alloy, tested in a 3.5 wt.% NaCl solution, is shown in Fig. 4 (c). For comparison with the annealed specimens, both the solutionized HEA and SS 304 L were also tested. Among the alloys, the solutionized HEA exhibited the least noble corrosion potential. However, its pitting potential exceeded that of SS 304 L by more than 100 mV. When comparing the spontaneous

passivity of all tested alloys, the passive corrosion current densities were found to be within a similar range.

Following annealing, the corrosion potential of the HEA became more noble. The 1 h, 2 h, and 50 h annealed specimens all exhibited similarly higher corrosion potentials, while the 4 h and 16 h samples showed slightly less noble values. The pitting potential also significantly increased after annealing, with the 1 h and 2 h specimens showing similar pitting potentials near 750 mVSCE. However, with extended annealing duration, the pitting potential progressively decreased, with the 50 h annealed sample approaching 550 mVSCE, indicating an increased susceptibility to pitting corrosion. Overall, the 1 h and 2 h annealing treatments resulted in the widest passive windows and the highest pitting potentials, thus offering the greatest resistance to localized corrosion. Metastable pitting was observed in both the SS 304 L and the 16 h annealed HEA specimen.

Table 1 shows the corrosion and pitting potentials of the HEA alloys annealed for different durations compared to conventional stainless steel.

Table 1 | Corrosion parameters for $Al_{0.3}CoCrFeNi$ alloys and conventional stainless steel

Sample	E_{corr} (mV)	E_pit (mV)
620-50 h	−125 ± 4	640 ± 125
620-16 h	−131 ± 9	637 ± 111
620-4 h	−131 ± 30	685 ± 19
620-2 h	−125 ± 4	759 ± 20
620-1 h	−125 ± 8	778 ± 28
Base	−147 ± 26	492 ± 87
SS304L	−105 ± 15	279 ± 22

The results indicate that the HEA alloy has significantly better corrosion resistance after annealing, regardless of the duration. Additionally, whether annealed or not, the corrosion resistance of the HEA alloy surpasses that of conventional stainless steel.

Figure 4 (d) illustrates the relationship between microstrain and corrosion resistance in $Al_{0.3}CoCrFeNi$ HEA alloys with varying annealing times. The data in Fig. 4 (b) shows that increased microstrain correlates with decreased corrosion resistance. Microstrain can introduce lattice defects and dislocations, which may serve as nucleation sites for corrosion initiation. These defects can accelerate corrosion by compromising the integrity of the passive layer.

Near-surface oxidation states after polarization

Figure 5 XANES spectra of the $Al_{0.3}CoCrFeNi$ alloy after PDP testing in 3.5 wt% NaCl solution, comparing the effects of different heat treatments on corrosion behavior. Since the photon energy of the main peak is similar across all three heat-treated samples before corrosion, only the data after corrosion is shown. XANES results include total electron yield (TEY) and total fluorescence yield (TFY) data, with TEY (probe depth: 5–10 nm) being surface-sensitive and TFY (probe depth: ~150 nm) being bulk-sensitive. As the TFY data shows minimal differences between corroded and uncorroded regions, only the TEY data is presented in Fig. 5.

The TEY spectrum in Fig. 5a for Cr shows a sharp peak in the base condition (0 h), indicating a significant surface oxide layer (e.g., Cr_2O_3) formed during corrosion[26]. This high intensity reflects Cr's high reactivity, establishing a protective oxide within the 5–10 nm surface region. After 2 h annealing at 620 °C, the peak intensity decreases slightly, suggesting an initial thinning or restructuring of the surface oxide, possibly due to microstructural changes or partial oxide dissolution. At 50 h, the intensity drops more noticeably, indicating a significant reduction in surface oxide

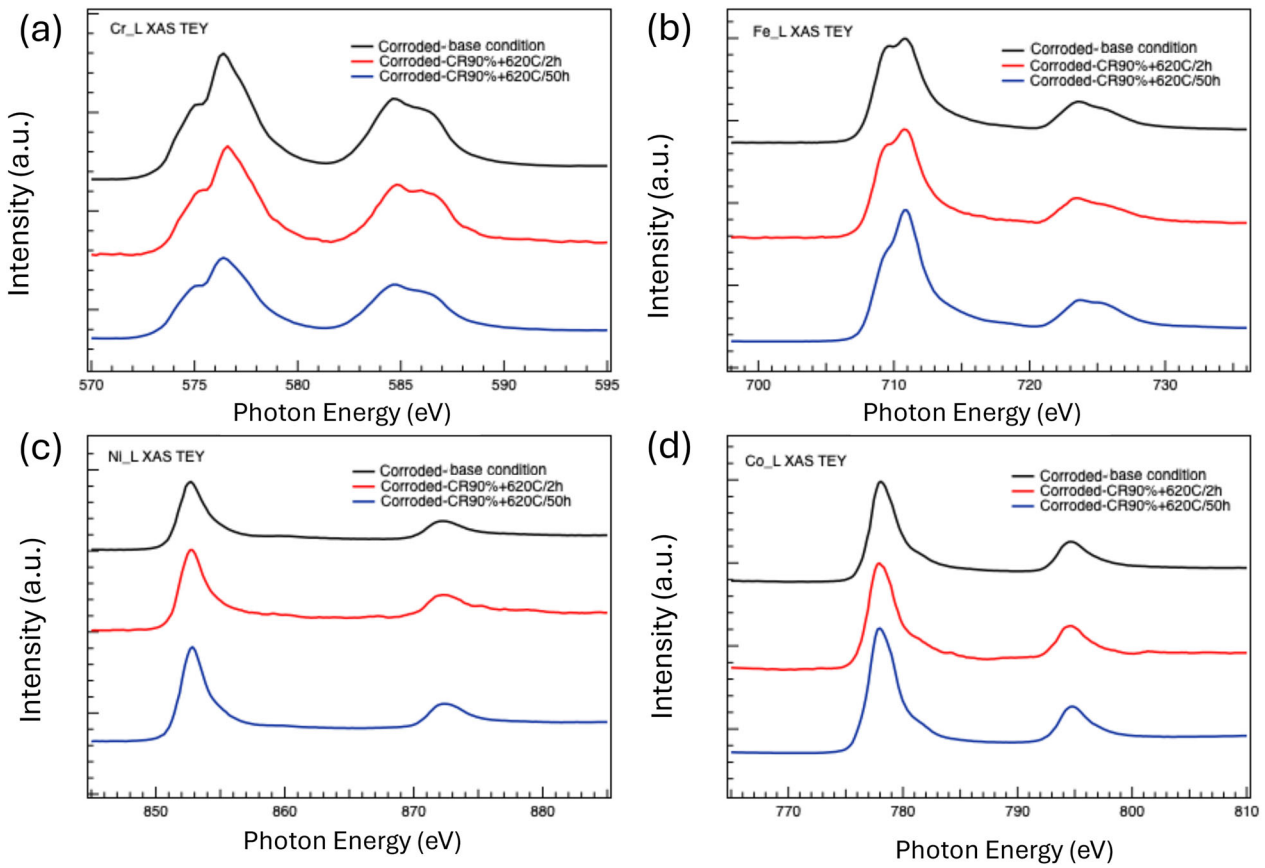


Fig. 5 | XAENS spectra of $Al_{0.3}CoCrFeNi$ alloy. a Ni-L, **b** Fe-L, **c** Cr-L, and **d** Co-L, for corroded areas across 3 annealing conditions (base condition, CR90 + 620 °C/2 h, and CR90 + 620 °C/50 h).

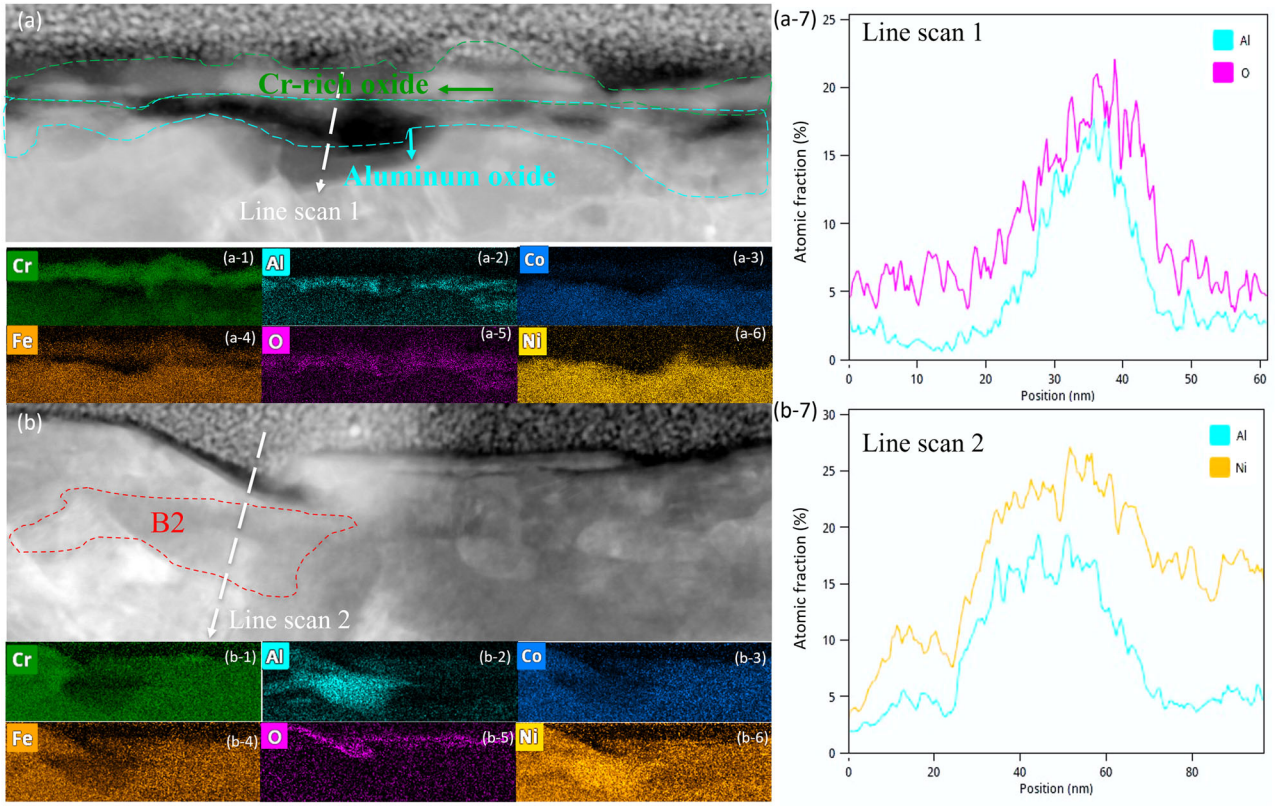


Fig. 6 | TEM images of $Al_{0.3}CoCrFeNi$ alloy after corrosion. a 2 h anneal: bilayer structure consisting of an inner Al_2O_3 layer as shown in EDS line profile in (a-7) and an outer Cr-rich oxide. **b** 16 h anneal: single Cr-rich oxide; Aluminum preferentially forms the phase within the matrix, as indicated by the accompanying EDS line profile in (b-7). Elemental maps (1–6) correspond to Cr, Al, Co, Fe, O and Ni, respectively.

concentration. This decreasing trend suggests that prolonged annealing weakens Cr's surface oxide stability, potentially due to diffusion of corrosive species into deeper layers or oxide breakdown, while the +3 oxidation state remains stable as no peak shifts are observed.

The TEY spectrum in Fig. 5b for Fe exhibits a prominent peak in the base condition (0 h), indicating surface oxidation (e.g., Fe_2O_3 or Fe_3O_4)[27]. After 2 h annealing at 620 °C, the peak intensity increases slightly, suggesting an enhancement in surface oxide formation or thickening, possibly due to improved Fe diffusion or oxide stabilization with initial heat treatment. At 50 h, the intensity rises further, reflecting a significant increase in surface oxide concentration. This increasing trend indicates that prolonged annealing strengthens Fe's surface oxide layer, potentially due to sustained reaction with the corrosive NaCl environment, with the $+2/+3$ oxidation state remaining stable as no edge shifts occur.

Based on the L-XAS TEY data in Fig. 5c, with peaks at 853.5 eV (L_3-edge) and 873 eV (L_2-edge) and a slight intensity increase at 50 h, the Ni is likely predominantly in an oxide state (e.g., Ni^{2+} as NiO) at the surface (5–10 nm), rather than metallic Ni^0. The stable intensity from 0 h to 2 h suggests an initial oxide layer formed during corrosion, and the slight increase at 50 h indicates minor oxide growth or thickening due to annealing. The edge positions (853.5 eV and 873 eV) support Ni^{2+}, and the intensity trend aligns with surface oxidation. The lack of a significant shift reflects a consistent oxidation state, with the 50 h increase driving limited oxide enhancement.

Based on the L-XAS TEY data in Fig. 5d, with peaks at 779 eV (L_3-edge) and 795 eV (L_2-edge) and an intensity increase at 50 h, the Co is likely predominantly in an oxide state (e.g., Co^{2+} as CoO, possibly Co^{3+} as Co_2O_3) at the surface (5–10 nm), rather than metallic Co^0. The stable intensity from 0 h to 2 h suggests an initial oxide layer formed during corrosion, and the increase at 50 h indicates enhanced oxide formation or thickening due to annealing. The L_3-edge at 779 eV aligns with Co^{2+}, and the intensity rise supports oxide growth, though a minor metallic contribution is possible if the oxide is thin. The lack of a significant shift may reflect a consistent oxidation state, with the 50 h increase driving further oxidation.

While XANES is highly effective for probing oxidation states in transition metals like Fe, Ni, and Co, it is significantly less sensitive to Al in HEA matrices. This is due to the low energy of the Al K-edge (Tender X-ray regime), where signal detection is often hampered by high background absorption from heavier matrix elements and limited probing depth in Total Electron Yield (TEY) mode. In contrast, XPS and TEM are more effective for Al characterization; XPS, in particular, excels at identifying Al oxidation states (e.g., Al^0 vs Al^{3+} through distinct binding energy shifts, even for thin surface oxides. While XANES provides unique insights into local coordination and bulk redox processes, XPS offers superior surface-specific chemical state information. Therefore, integrating these complementary techniques is essential for a comprehensive understanding of corrosion and phase stability in Al-containing HEAs.

The TEY–TFY contrast confirms that these changes originate within the near-surface region. The reduced Cr TEY intensity at 50 h is consistent with Cr being tied up in σ, while the increased Fe/Ni TEY signals indicate a shift toward Fe/Ni-rich oxides when Al_2O_3 is absent. The lack of detectable Al signal aligns with Al being locked into B2 at long annealing times.

Corrosion product morphology through microstructure characterization

Figure 6 shows the TEM images of the different heat-treated $Al_{0.3}CoCrFeNi$ HEA alloys after corrosion. For short annealing, two distinct layers are observed on the surface of the CR90-620 °C/2 h sample as shown in Fig. 6(a). Note that the specimens were subjected to anodic polarization up to the pitting potential, resulting in localized breakdown of the passive film and initiation of stable pitting corrosion. Consequently, the protective oxide

layers originally present on the surface have been extensively damaged or dissolved in the pitted regions. The observed surface features (e.g., corrosion product aggregates) are characteristic of post-pitting degradation and do not represent the intact passive film formed under open-circuit or early-stage polarization conditions. These images serve to illustrate the morphology and subsurface damage induced by pitting attack rather than the structure of the protective film.

The outermost layer is rich in Cr (60 at%), while the second layer consists of Al_2O_3, as confirmed by characteristic Al 2p and O 1 s binding energies in XPS spectra and composition from EDS analysis in Table 2.

In contrast, the CR90-620 °C/16 h sample does not exhibit the presence of Al_2O_3 as shown in Fig. 6 (b). Instead, a Cr-rich oxide layer forms on the surface. This reflects a transition into a thermodynamically driven regime where coarsened B2 and σ phases sequester Al from the matrix. As a result, Al_2O_3 formation is suppressed, and the passive film becomes Cr-dominated. Furthermore, the matrix of the 16 h annealed sample contains B2 phases, with B2 phases forming along specific grain boundaries—phases that are not observed in the 2 h annealed sample. For the 2 h annealed sample, the rapid formation of Al_2O_3 suggests a kinetic pathway where aluminum preferentially reacts with oxygen rather than diffusing to form the B2 phase. This preference indicates that the alloy may not reach the equilibrium state required to stabilize the B2 phase during the shorter annealing time.

Li et al.[13] proposed that in $Al_{1.0}CoCrFeNi$ and $Al_{1.3}CoCrFeNi$ alloys, Al reacts with NaCl to form $AlCl_3$, which subsequently leads to the formation of a protective Al_2O_3 layer on the surface. This mechanism effectively protects the alloy from corrosion. In the current study, the presence of Al_2O_3 in the CR90-620 °C/2 h sample suggests that it also plays a protective role, contributing to better corrosion resistance in shorter annealing times (1–2 h) compared to longer times (16 h or more). The presence of a Cr-rich layer above the Al_2O_3 has also been reported in previous studies. Gwalani et al.[22] used a combination of in situ atom probe tomography and thermo-kinetic treatment applying preferential interactivity parameter approach to investigate the oxidation mechanism/sequence. They reported that the early stages of oxidation can be interpreted through a multi-pronged coupling of thermodynamic parameters such as atomic size, cohesive energy, electro-negative and so on.

An aluminum oxide (Al_2O_3) layer tends to form first on HEAs due to the higher affinity of aluminum for oxygen, leading to its preferential oxidation over elements like Cr, Fe, Co, and Ni. According to the Ellingham diagram, aluminum has a significantly lower Gibbs free energy of oxidation than these elements, making the formation of Al_2O_3 thermodynamically more favorable. This behavior is particularly advantageous in HEAs, as the rapid formation of a protective Al_2O_3 layer can enhance the oxidation resistance of the material.

Figure 7 shows the Cr and Al signals in the differently heat-treated HEAs after corrosion. The data indicate that protective oxide layers containing Cr_2O_3 and Al_2O_3 formed after corrosion. All raw XPS spectra are provided in the supplementary information (Figs. S5 and S6) for comprehensive detail. It appears that Al_2O_3 reaches its maximum intensity in the HEA after cold rolling and annealing at 620 °C for 2 h. However, the intensity of Cr_2O_3 decreases after corrosion in the HEA subjected to longer annealing.

Table 2 | Atomic ratio of metals in $Al_{0.3}CoCrFeNi$ HEA alloy (a) annealing at 620 °C for 2 h and (b) 16 h after corroding in 3.5 wt % NaCl solution

	Atomic Ratio of metals	Al	Cr	Fe	Co	Ni
(a)	620 °C-2 h (Al_2O_3)	9.7	2.9	1.0	1.2	1.0
	620 °C-2 h Cr-rich oxide	0.6	3.4	1.0	0.7	0.3
(b)	620 °C-16 h Cr-rich oxide	0.6	2.3	1.0	1.0	1.2

Note: Atomic ratios are normalized relative to Fe (Fe = 1.0).

Change in corrosion mechanisms as a function of microstructural change

Figure 8 shows the schematic illustration of the effect of annealing time on corrosion behaviors of $Al_{0.3}CoCrFeNi$ HEA alloy. Before corrosion, annealing at 620 °C for 2 h results in partial recrystallization, especially in areas that experienced significant strain during cold rolling. These recrystallized regions exhibit equiaxed grains with low dislocation density. However, most regions remain un-recrystallized due to the high degree of

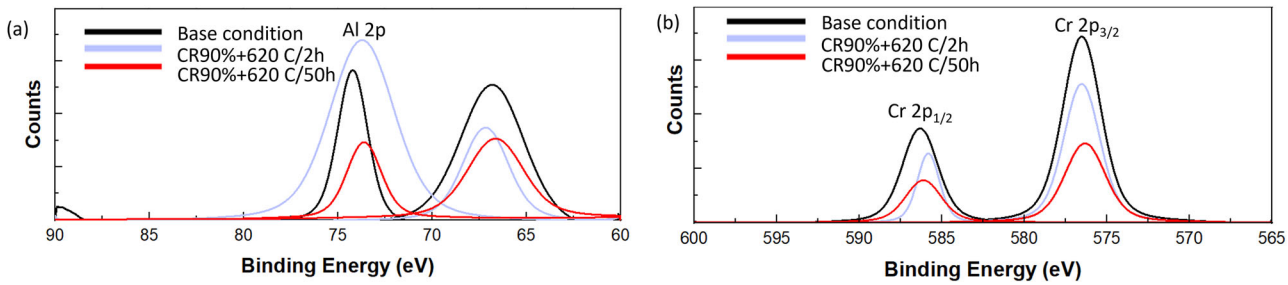
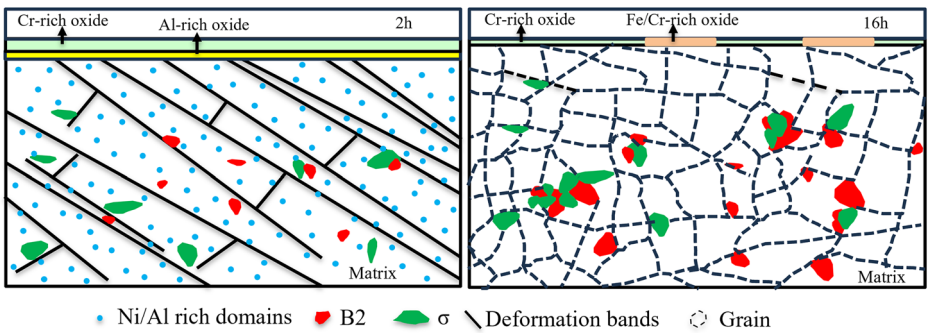


Fig. 7 | Chemical states of passive films analyzed via XPS spectra. XPS spectra of **a** Al 2p and **b** Cr $2p_3/_2$ peaks for the base alloy and specimens annealed 2 h and 50 h, post-corrosion. Al_2O_3 intensity maximizes after 2 h, whereas Cr_2O_3 dominates in the base condition.

Fig. 8 | Schematic of annealing time effects on corrosion mechanisms in Al0.3CoCrFeNi. Short-time annealing retains matrix, enabling an Al_2O_3-first passive film, whereas long-time annealing partitions Al into B2.



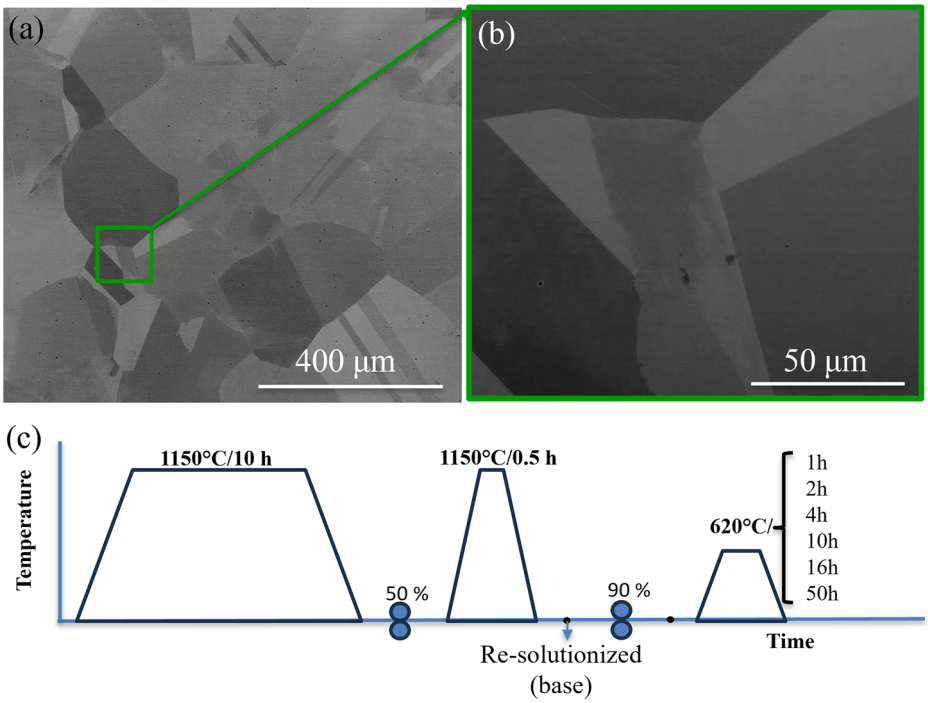


Fig. 9 | Initial microstructures and thermo-mechanical processing schedule. a Secondary-electron image of the alloy in the re-solutionized base state, showing equiaxed FCC grains; **b** higher-magnification view of the boxed region in (**a**); **c** Thermomechanical schedule used in this study: dual solutionizing, sequential 50% and 90% cold-rolling, followed by isothermal holds at 620 °C.

plastic deformation caused by cold rolling, retaining elongated grains and a higher dislocation density. Moreover, Ni/Al-rich domains act as nuclei for B2 phase formation.

After corrosion, NaCl solution dissolves the metal matrix, leading to the formation of a protective Al_2O_3 oxide layer due to its thermodynamic stability. The Cr-rich phase forms on top of Al_2O_3 because chromium also has lower redox potential compared to other metal elements (Fe, Co and Ni)[22] and higher diffusion coefficients in aluminum oxide[28].

Roy et al.[28] studied cationic and anionic diffusion through stable aluminum oxides in a model HEA using atomistic simulations. They found that metal ions such as Cr, Fe, Co, and Ni have higher diffusion coefficients than Al or O ions, indicating that these metal ions move more easily or rapidly than Al or O ions. This finding aligns with our observations, where we identified a Cr-rich phase on top of the Al_2O_3 layer.

For longer annealing time at 16 h, more regions were recrystallized compared to the 2-h annealing condition, primarily exhibiting FCC phases. In addition, B2 and sigma phases formed in some regions due to their thermodynamic stability. After corrosion, due to the formation of the B2 phase, aluminum preferentially formed B2 in the matrix rather than Al_2O_3 on the surface, compared to the 2 h condition. Cr_2O_3 and $FeCr_2O_4$ spinel oxides were formed on the surface due to their thermodynamic stability[29]. The previous work on stainless steels and nickel-based alloys in simulated pressurized water reactor conditions has consistently shown the presence of these stable oxide phases contributing to corrosion performance[30–32].

This microstructural evolution reveals a critical transition point in the alloy's performance. While the short-term annealing (1–2 h) optimizes the balance between mechanical strength and corrosion resistance by facilitating Al-rich oxide films, the proliferation of B2 and sigma phases at longer durations depletes the Al available for protective oxide formation. Despite this shift, the Al0.3CoCrFeNi HEA maintains superior corrosion resistance compared to conventional stainless steel. Ultimately, these findings highlight that optimizing the heterogeneous microstructure—specifically the ratio of recrystallized regions to intermetallic phases—is the primary driver for enhancing HEA performance in corrosive environments. Moving forward, this mechanistic framework will be extended to elevated-temperature critical pitting measurements to evaluate passivation stability under aggressive oxidizing chloride environments.

Methods

Alloy fabrication and thermomechanical processing

The $Al_{0.3}CoCrFeNi$ alloy was synthesized via the traditional arc melting method with an Arcast arc melter (Arc 200)[33]. The buttons were inverted five times and remelted to ensure complete homogeneity. Figure 9 summarizes all subsequent thermomechanical processing after alloy synthesis. First, a solutionizing treatment at 1150 °C for 10 h was performed in a vacuum furnace to homogenize the material and dissolve any pre-existing precipitates, resulting in a single-phase FCC microstructure. Next, the material was subjected to 50% cold rolling to introduce significant plastic strain and increase dislocation density. A second solutionizing step at 1150 °C for 0.5 h was then performed after encapsulating the samples in titanium foil with a tantalum getter, followed by water quenching to facilitate recrystallization. Figure 9 (a) and (b) show the secondary electron images in the re-solutionized (base) condition, exhibiting a single-phase FCC microstructure. Further deformation through 90% cold rolling increased the dislocation density and enhanced hardness. Finally, the samples were isothermally annealed at 620 °C for periods ranging from 1 to 50 h.

Microstructural characterization

Scanning electron microscopy (SEM) and electron backscatter diffraction (EBSD) maps were prepared using a FEI Nova NanoSEM equipped with an EBSD detector. X-ray diffraction (XRD) studies were conducted at room temperature using a Rigaku SmartLab X-ray Diffractometer with Cu Kα radiation ($\lambda = 1.54$ Å, 45 kV, 44 mA) to determine the phase composition. Specific samples for transmission electron microscopy (TEM) were prepared using a FEI Nova 200 dual-beam focused ion beam (FIB) system and analyzed in a ThermoFisher Talos F200X microscope operating at 200 kV.

Atom probe tomography (APT) specimens were prepared using a site-specific focused ion beam (FIB) lift-out technique in an FEI Helios dual-beam FIB-SEM. A Pt capping layer was deposited to protect against Ga ion damage. Needle-shaped tips were fabricated from the uncrystallized region of the HEA alloy (CR90 followed by annealing at 620 °C for 1 h). Final needle sharpening involved annular milling with progressively reduced ion beam currents (30 nA down to 10 pA) and low-kV (2–5 kV) cleaning steps, resulting in tips with apex radii of ~50–100 nm and minimized Ga ion implantation.

APT analysis was performed on a CAMECA LEAP 4000X HR system using a 355 nm UV laser (200 pJ, 200 kHz) at a specimen base temperature of 45 K, with a detection rate of 0.003 ions/pulse. The chamber pressure was maintained below 2×10^{-11} Torr. Data reconstruction and comprehensive quantitative analysis—including 3D compositional mapping, 1D concentration profiles, proximity histograms, and cluster analysis—were conducted using CAMECA IVAS 3.8.2 software, with a detector efficiency of ~36%.

X-ray Absorption Near Edge Structure (XANES) data were analyzed using SIXPACK software, with the photoelectron energy origin (E_0) determined by the first inflection point of the absorption edge jump. For calibration, the main peak of the spectra was aligned with literature values for the respective transition metals. Normalization of the spectra was performed by adjusting the pre-edge area to 0 and the post-edge area to 1, ensuring consistency and comparability between different spectra.

X-ray Photoelectron Spectroscopy (XPS) characterization was carried out using a spherical capacitance analyzer with advanced detector technology and a high-performance Al X-ray monochromator source. All survey spectra scans were taken at a pass energy of 58.7 eV. The data were acquired overnight and analyzed using Perkin-Elmer XPS systems equipped with SCAs and Omni FOCUS™ lenses.

Mechanical testing

Microhardness testing was performed using a standard Vickers microhardness tester with a 500 g load applied for 10 s. An average of 10 indents per condition was considered to ensure accuracy.

Electrochemical measurements

Electrochemical tests were conducted using a Biologic VMP-300 potentiostat controlled by EC-lab software in a conventional three-electrode cell. The sample served as the working electrode with an exposure area of approximately 0.079 cm^2, a platinum mesh was used as the counter electrode, and a saturated calomel electrode (SCE) served as the reference electrode. Prior to polarization tests, the samples were immersed in a 3.5 wt% NaCl solution for 3 h to stabilize the open circuit potential.

Data availability

All data were available in the main text or the supplementary materials.

Received: 27 November 2025; Accepted: 18 May 2026;
Published online: 02 June 2026

References

1. Miracle, D. B. Critical assessment 14: high entropy alloys and their development as structural materials. *Mater. Sci. Technol.* **31**, 1142–1147 (2024).
2. Stepanov, N. D. et al. Effect of Al on structure and mechanical properties of AlxNbTiVZr (x = 0, 0.5, 1, 1.5) high entropy alloys. *Mater. Sci. Technol.* **31**, 1184–1193 (2015).
3. Kumar, A. & Gupta, M. An insight into evolution of light weight high entropy alloys: a review. *Metals* **6**, 199 (2016).
4. Sonal, S. & Lee, J. Recent advances in additive manufacturing of high entropy alloys and their nuclear and wear-resistant applications. *Metals* **11**, 1980 (2021).
5. Yeh, J. W. et al. Nanostructured high-entropy alloys with multiple principal elements: novel alloy design concepts and outcomes. *Adv. Eng. Mater.* **6**, 299–303 (2004).
6. Cantor, B. et al. Microstructural development in equiatomic multicomponent alloys. *Mater. Sci. Eng. A*. **375-377**, 213–218 (2004).
7. Gwalani, B. et al. Tensile yield strength of a single bulk Al0.3CoCrFeNi high entropy alloy can be tuned from 160 MPa to 1800 MPa. *Scr. Mater.* **162**, 18–23 (2019).
8. Miracle, D. B. & Senkov, O. N. A critical review of high entropy alloys and related concepts. *Acta Mater.* **122**, 448–511 (2017).
9. Shi, Z. J. et al. Effect of thermally induced B2 phase on the corrosion behavior of an Al0.3CoCrFeNi high entropy alloy. *J. Alloy. Compd.* **903**, 163886 (2022).
10. Qiu, Y. et al. Corrosion of high entropy alloys. *npj Mater. Degrad.* **1**, (2017).
11. Shi, Y. et al. Corrosion of Al CoCrFeNi high-entropy alloys: Al-content and potential scan-rate dependent pitting behavior. *Corros. Sci.* **119**, 33–45 (2017).
12. Gwalani, B. et al. Compositionally graded high entropy alloy with a strong front and ductile back. *Mater. Today Commun.* **20**, 100602 (2019).
13. Li, L. et al. Al CoCrFeNi high entropy alloys with superior hot corrosion resistance to Na2SO4 + 25% NaCl at 900. *C. Corros. Sci.* **187**, 109479 (2021).
14. Firouzdor, V. et al. Corrosion of a stainless steel and nickel-based alloys in high temperature supercritical carbon dioxide environment. *Corros. Sci.* **69**, 281–291 (2013).
15. Zhang, X. et al. Influence of remelting and annealing treatment on corrosion resistance of AlFeNiCoCuCr high entropy alloy in 3.5% NaCl solution. *J. Alloy. Compd.* **775**, 565–570 (2019).
16. Lu, P. et al. Computational materials design of a corrosion resistant high entropy alloy for harsh environments. *Scr. Mater.* **153**, 19–22 (2018).
17. Liang, J. et al. Corrosion resistance and mechanism of high-entropy alloys: A review. *Mater. Corros.* **75**, 424–432 (2024).
18. Chen, M. et al. Phase, microstructure and corrosion behaviour of Al(0.3)FeCoNiCr(x) high-entropy alloys via Cr addition. *Materials*. **17**, (2024).
19. Sahu, S. et al. Localized corrosion behavior of non-equiatomic NiFeCrMnCo multi-principal element alloys. *Electrochim. Acta* **354**, 136749 (2020).
20. Liu, Z. et al. Microstructure, mechanical properties and corrosion resistance of direct energy deposited AlCu0.25CoCrFeNi2.1 high entropy alloy: Tailored by annealing heat treatment. *Mater. Charact.* **213**, 114035 (2024).
21. Martin, A. & Thuo, M. Predicting emergence of nanoscale order in surface oxides through preferential interactivity parameter. *ACS Nano* **18**, 6740–6747 (2024).
22. Gwalani, B. et al. Mechanistic understanding of speciated oxide growth in high entropy alloys. *Nat. Commun.* **15**, 5026 (2024).
23. Lee, C. P. et al. Enhancing pitting corrosion resistance of AlxCrFe1.5MnNi0.5 high-entropy alloys by anodic treatment in sulfuric acid. *Thin Solid Films* **517**, 1301–1305 (2008).
24. Wilms, M. E. et al. The effect of σ-phase precipitation at 800 °C on the corrosion resistance in sea-water of a high alloyed duplex stainless steel. *Corros. Sci.* **36**, 871–881 (1994).
25. Shang, X.-L. et al. Effect of Mo addition on corrosion behavior of high-entropy alloys CoCrFeNiMox in aqueous environments. *Acta Metall. Sin.* **32**, 41–51 (2019).
26. Seong, S. et al. Experimental evidence for mixed-valent Cr ions in half-metallic CrO2: Temperature-dependent XMCD study. *J. Magn. Magn. Mater.* **452**, 447–450 (2018).
27. Fonin, M. et al. Surface electronic structure of the Fe3O4(100): evidence of a half-metal to metal transition. *Physical Rev. B*. **72**(2005).
28. Roy, I., Ray, P. K. & Balasubramanian, G. Diffusion of multi-principal elements through stable Cr2O3 and Al2O3 scales. *Materialia* **24**, 101497 (2022).
29. Puigdomenech, B.B.a.I., Pourbaix diagrams for the ternary system of Fe-Cr-Ni. *Corrosion*. **55**): p. 1077-1087.
30. Tsai, F.Y. Corrosion Sensitivity of Stainless Steels in Pressurized Water Reactor Water Chemistry: Can KOH replace LiOH in PWRs. *Doctoral dissertation, North Carolina State University* https://repository.lib.ncsu.edu/items/937cd4c1-72a3-4d73-b5d8-8def6b7670ac, (2022).
31. Tsai, F.-Y. et al. Corrosion sensitivity of nickel-based Alloy Inconel 600 in pressurized water reactor water chemistry: Can KOH replace LiOH?. *Corros. Sci.* **255**, 113052 (2025).

32. Tsai, F.-Y. et al. Effect of irradiation on the corrosion of 304 stainless steel in pressurized water reactor (PWR) simulated water chemistry. *Corros. Sci.* **240**, 112454 (2024).
33. Gwalani, B. et al. Modifying transformation pathways in high entropy alloys or complex concentrated alloys via thermo-mechanical processing. *Acta Mater.* **153**, 169–185 (2018).

Acknowledgements

TEM characterization was performed at the Analytical Instrumentation Facility (AIF) at North Carolina State University, which is supported by the State of North Carolina and the National Science Foundation (award number ECCS-1542015). This work made use of instrumentation at AIF acquired with support from the National Science Foundation (DMR-1726294). The AIF is a member of the North Carolina Research Triangle Nanotechnology Network (RTNN), a site in the National Nanotechnology Coordinated Infrastructure (NNCI). The XANES measurements were carried out on BL8.0.1 and used resources of the Advanced Light Source, which is a DOE Office of Science User Facility under contract no. DE-AC02-05CH11231. The research was supported (in part) by ONR under Grant N00014-23-1-2758 and Alice Pandaleon was supported by the NSF-funded MAT-DAT REU Site (DMR-2150360). The funders had no role in study design, data collection and analysis, decision to publish, or preparation of the manuscript.

Author contributions

F.Y.T., A.P., S.O., A.M., A.Pa., F.I., M.L., Z.Z. and M.J.U. performed experiments, data collection, and preliminary analysis. J.G., M.M.T., R.G., R.B. and E.K. contributed to the interpretation of results and methodology development. F.Y.T., A.P., S.O., A.M., A.Pa., F.I. and M.L. assisted with data curation, visualization, and figure preparation. B.G. led project conceptualization, experimental design, and overall supervision. F.Y.T. and B.G. prepared the initial manuscript draft. All authors (F.Y.T., A.P., S.O., A.M., A.Pa., F.I., M.L., M.J.U., Z.Z., J.G., M.M.T., R.G., R.B., E.K., B.G.) reviewed and approved the final manuscript.

Competing interests

The authors declare no competing interests.

Additional information

Supplementary information The online version contains supplementary material available at https://doi.org/10.1038/s41529-026-00818-4.

Correspondence and requests for materials should be addressed to Bharat Gwalani.

Reprints and permissions information is available at http://www.nature.com/reprints

Publisher's note Springer Nature remains neutral with regard to jurisdictional claims in published maps and institutional affiliations.

Open Access This article is licensed under a Creative Commons Attribution-NonCommercial-NoDerivatives 4.0 International License, which permits any non-commercial use, sharing, distribution and reproduction in any medium or format, as long as you give appropriate credit to the original author(s) and the source, provide a link to the Creative Commons licence, and indicate if you modified the licensed material. You do not have permission under this licence to share adapted material derived from this article or parts of it. The images or other third party material in this article are included in the article's Creative Commons licence, unless indicated otherwise in a credit line to the material. If material is not included in the article's Creative Commons licence and your intended use is not permitted by statutory regulation or exceeds the permitted use, you will need to obtain permission directly from the copyright holder. To view a copy of this licence, visit http://creativecommons.org/licenses/by-nc-nd/4.0/.

© The Author(s) 2026